Northern Hemisphere Blocking Highs in a Solar Radiation Management Scenario

Bárbara Delgado

December 3, 2019

Abstract

Solar Radiation Management (SRM) has been rising in popularity as a potential method to offset climate warming due to increased greenhouse gases (GHG). The response of climate to geoengineering remains a challenge and has been studied under idealized experiment design in the Geoengineering Model Intercomparison Project (GeoMIP). The GCM CESM(WACCM) Geoengineering large ensemble (GLENS) was created to help gain insight into geoengineering impacts when stratospheric sulphate is injected in the tropics as to keep a set of surface temperature goals in 2020 levels. Blocking highs are a high impact synoptic-scale feature, associated with cold-spells and heat-waves in Europe. For this thesis, the change in blocking occurrence, under the GLENS SRM scenario, was studied using two meridional geopotential inversion methods: Tibaldi and Molteni (1990) and Barnes et al. (2012). It was found that overall blocking frequency increases in relation to a control (RCP8.5) scenario, and keeps other regional and seasonal features in relation to starting period, unlike the control. These changes have a high correlation to the NAM behaviour. Persistence and extent of blocks show no significant change.

1. Introduction

Climate warming poses many risks, from biodiversity loss to sea level rise. As climate change mitigation measures (The Paris Agreement, 2015) are looking unlikely to meet the goal of keeping global temperatures below the 2°C target, the pertinence of research into climate engineering, or geoengineering, increases (MacMartin and Kravitz, 2019a). Various techniques to artificially cool the planet have been proposed, and they can typically belong to one of two main categories of geoengineering (Lenton and Vaughan, 2009). The first is Solar Radiation Management (SRM), referring to methods that aim to reduce the incoming solar radiation, and they are typically associated with surface or cloud albedo change, either regionally or globally. The second category is Greenhouse Gas Removal (GGR), which refers to methods that remove greenhouse gases from the atmosphere, such as Afforestation or Ocean Fertilisation. Even though SRM methods cannot replace mitigation strategies, SRM has the potential to slow down the global temperatures increase in a shorter timescale (MacMartin and Kravitz, 2019b). For this thesis, a method of SRM known as Stratospheric Aerosol (SA) geoengineering is explored. SA has been a proposed strategy for many years, and it is based on the knowledge that radiative forcing is offset when stratospheric volcanic eruptions occur. When Mount Pinatubo erupted in 1991, in the Philippines, the global temperature was cooled by about 0.5°C in the following 2 years and injected around 10Tg of SO_2 into the stratosphere. Satellite observations allowed a better estimation of the Pinatubo eruption radiative forcing than previous eruptions (Minnis et al., 1993). In this sense, albeit rare, eruptions

provide a natural source of observations that help constrain the climate response to aerosol injection.

The question is then, what would happen in a geoengineering scenario, and which climate change impacts can be ameliorated and which geoengineering impacts would be worse. The objective of this thesis is to investigate the change in blocking events under a geoengineering scenario. *Blocking highs*, *blocking anticyclones*, or simply *blocks* are a meteorological phenomenon that blocks or obstructs the typical synoptic scale features (transient) around the mid-latitude jet stream. Blocking Highs are essentially characterized by their quasi-stationarity, lasting from a few days to several weeks, that upset the typically westerly flowing winds in the mid-latitude region. This can lead to extreme events such as heatwaves in the summer on the western side (upstream) and cold spells in the winter on the eastern side (downstream) of the Block, due to anomalous (stationary) meridional flow. Furthermore, the weak winds associated with a quasi-stationary high-pressure system, and high temperatures in the summer can lead to the deterioration of air quality (ozone increase, decreased pollutant deposition...), as well as droughts and increased fire risk. Hence, blocking represents a high impact weather phenomena in the mid-latitudes and has been associated with the European summer heatwaves, like the one in 2010 that severely hit Russia (Matsueda, 2011). Additionally, blocks might be responsible for the change of path (steering) of other high-impact weather systems, such as hurricanes (Barnes et al., 2013).

Not all blocking events are created equal, and three types are commonly described in literature (Woollings et al., 2018). Dipole Blocks, or Rex blocks (after Rex (1950)), resemble a "figure 8" and are associated with Rossby wave breaking events. When an extended ridge folds either cyclonic or anticyclonically (and breaks) creates a meridional potential vorticity (PV) reversal, with an anticyclonic core on the poleward side, and a cyclonic core on the equatorward side. Planetary wave breaking in the "Middleworld" region, the isentropic levels of upper troposphere in the low latitudes and low stratosphere in the mid-high latitudes, is associated with isentropic mixing between the tropical and polar regions. The dynamical tropopause is defined as the 2 potential vorticity unit level, or PVU (from Ertel's Potential Vorticity equation and equal to 2×10^{-6} m^2 K s^{-1} kg^{-1}). Most of the wave breaking events occur in the mid-latitudes jet exit regions, at the Eastern side of the Atlantic and Pacific basins, where weaker meridional PV gradients are observed (van Delden, 2017). Omega blocks are formed when a poleward displaced subtropical (low-PV) mass of air forms an anticyclonic anomaly in the middle latitudes and is partially contoured by isobars, resembling the omega letter shape. Mid-latitude stationarity can also be achieved when a large amplitude Rossby wave ridge, with low-PV and anticyclonic in relation to the surroundings, reaches zero phase-speed in the middle latitudes. The 2PVU level and the 500 hPa geopotential height (Z500) are typically used to observe meridional gradient reversals associated with blocks. Since potential vorticity and potential temperature are (approximately) conserved by air parcels, the displacement of tropical air is easily identified in the 2 PVU level. The low PV can be tracked on isentropic levels, or alternatively, high potential temperature on constant PV levels. The three block types are shown in Figure 1, as well as cyclonic and anticyclonic wave breaking events.

Although blocks are typically located at jet exit regions, blocking forcing arises not only from the tropics, but also from purely middle latitude dynamics, and sea-surface mean state. Blocks are related to both barotropic planetary waves and baroclinic waves associated with synoptic-scale weather events, and the preferential forcing varies regionally. The blocking establishment can originate from the interaction of different wavelength Rossby waves, or by interaction of Rossby waves with the mean flow. It can also sometimes be associated with rapid cyclogenesis events, as cyclones slowly move poleward (conserving its properties) and lead to ridge building downstream.

Furthermore, there seems to be a connection between polar stratosphere dynamics and blocking, for example related to polar vortex strength and sudden polar stratospheric warming (Vial et al., 2013). Maintenance of the blocking event is related to vorticity anomaly feeding into the established block. This vorticity anomalies can be associated to positive feedback of synoptic scale phenomena, or by further forced wave breaking, by the over-stretching of Rossby waves upstream of the block with the diffluent flow around the event. Additionally, diabatic processes in poleward moving systems intensify the anticyclonic anomaly, with higher level outflow (greater horizontal PV gradient at higher levels). The diabatic effect advects the dynamical tropopause and structure further poleward. When the maintenance process is disrupted, the low PV anomaly is absorbed by the the tropical low PV pool.

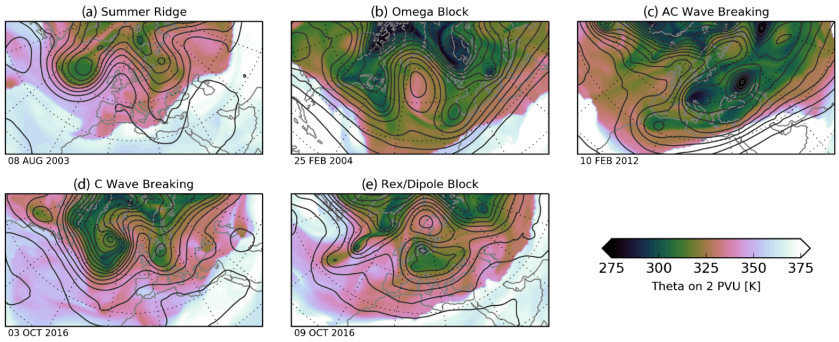

Figure 1. Figure taken from Woollings et al. (2018), displaying the types of blocks described above, in the North Atlantic region. ERA-Interim reanalysis data from the labeled days, showing in colour the potential temperature θ in the 2PVU level, and contour lines for the 500hPa geopotential height (60m spacing).

Blocking frequency in the North Atlantic has been linked to the North Atlantic Oscillation (NAO) negative phase. A possible factor for this connection is related to the weakening of the jet, favouring the splitting of the jet and the formation of a diffluent background flow (Luo, 2005). A more general Northern Hemisphere (NH) index is the North Annular Mode (NAM), or Arctic Oscillation (AO), mainly expressing the NAO behaviour in wintertime. The NAM index is defined as the normalised difference of the zonal-mean sea level pressure (SLP) between 35N and 65N. These two latitude belts are called the annular belts of action (ABAs), and the SLPs represent the relative strengths of the subtropical high and sub-polar low (Li and Wang, 2003). The NAM reflects then the intensity of the surface zonal wind anomalies over latitudes within the range of the mid-latitude and high-latitude ABAs. Positive values of the NAM, with higher anomalies on the pressure fields and increased gradient, are associated with a strong NH Polar jet and vortex, an enhanced Ferrel cell circulation and a weakened subtropical jet. During a positive phase the mid-latitude jet is predominantly zonal, while during negative phases the jet meanders more and the meridional flux of mass is enhanced.

The climate is a complex and non-linear system and, albeit associated with uncertainties, models remain the best method to study climate response (MacMartin and Kravitz, 2019b). Geoengineering research and experimental design are actively investigated under the Geoengineering Model Intercomparison Project (GeoMIP) (Kravitz et al., 2018). There are several scales associated with aerosol feedback processes, and models have the limitation of not being able to resolve both cloud/eddy scale processes as well as general global circulation. Also, different aerosol size has distinct and complex aerosol growth (microphysical processes scheme), implying a large radiative forcing uncertainty. Furthermore, many of the known impacts have been investigated using a changed albedo as a proxy in models. They provide useful information about global features of geoengineering impact, as for example polar amplification (higher warming in the poles than in the tropics) or the asymmetric cooling of both hemispheres. The Geoengineering Large Ensemble

(GLENS) project was created with the aim of generating a climate model geoengineering ensemble to study regional impacts in a high carbon emission scenario. It includes comprehensive middle atmosphere chemistry in a fully coupled global climate model (Community Earth System Model). CESM has been both validated against climatology observations as well as observations after the Pinatubo eruption in 1991 (Mills et al., 2017), making it convenient for SO_2 geoengineering studies (Tilmes et al., 2018). In this project, the high-resolution daily output of the GLENS project is used to track blocking highs in the geoengineering climate versus a high carbon emission climate scenario. The dataset is described in section 2.1.

Several methods of tracking have been developed (Barriopedro et al., 2010), focusing on the different features of blocking events. For this project, two (absolute field) meridional flow reversal methods are applied to the 500hPa geopotential height, to track blocking highs in the Northern Hemisphere. The first was developed by Tibaldi and Molteni (1990) and the second by Barnes et al. (2012). Both methods and the associated challenges of block tracking are described in section 2.2 (Methods). Section 2 presents then the data and methods, followed by the results and discussion in section 3. Section 4 presents the final conclusions from this work.

2. Data and Methods

2.1. Data

The dataset used in this project is an ensemble created for the Stratospheric Aerosol Geoengineering Large Ensemble (GLENS) Project. The simulations are performed with the fully coupled Climate Community Earth System Model (CESM) version 1 and the Whole Atmosphere Community Climate Model (WACCM) - CESM1(WACCM). The atmosphere component, WACCM, has the same physics as Community Atmosphere Model version, with a Quasi-Biennial Oscillation (QBO) and comprehensive description of sulphate aerosol chemistry both in the stratosphere and troposphere (Mills et al., 2017). The aerosol chemistry scheme includes aerosol conversion from SO_2, microphysical growth and sedimentation, and is interactive with radiation and dynamics. The model was successfully validated against observations of aerosol optical depth after the 1991 Pinatubo eruption (Mills et al., 2016). All model components are listed in Table 1 as described in (Tilmes et al., 2018). The output data is made available to the community through the NCAR Earth System Grid (ESG), and it can be downloaded from the project page at `www.cesm.ucar.edu/projects`. Results and papers obtained with this dataset can also be found on the GLENS project page.

Model Component	Version
Atmosphere	Whole Atmosphere Community Climate Model (WACCM)
Aerosol	Model Aerosol Model (MAM3)
Land	Community Land Model (CLM4.5)
Biogenic Emissions	Model of Emission of Gases and Aerosols from Nature (MEAGAN2.1)
Sea Ice	Los Alamos National Laboratory Sea Ice Model (CICE4)
Ocean	Parallel Ocean Program (POP2)

Table 1. GLENS model components for CESM1. For more details and specific model references see Tilmes et al. (2018).

To investigate regional and global impacts of geoengineering versus natural variability of the system, the GLENS project runs a 20-member ensemble of the CESM model in a high greenhouse gas concentration scenario from 2020 to 2100. The model follows the Representative Concentration Pathway 8.5 (RCP8.5) with SO_2 injection as the geoengineering scenario (Geo). In addition, a

20-member ensemble in an RCP8.5 scenario, with no geoengineering, is run as the control, from 2010 to 2100. The high forcing was chosen to create a better contrast between climate variability and forced climate change with increasing injections. Each member of the geoengineering scenario diverges from a control member in 2020. The control members are initialised with slightly different atmosphere conditions from a historic spin-up up to 2005 and RCP8.5 to 2010 from CESM(WACCM) used in Mills et al. (2017). The conditions are taken from various January 1st between 2008 and 2012 plus small air temperature perturbations (10^{-14}). The land, sea ice and ocean initial states are taken from 2010 values of an ensemble member of the CESM Large ensemble project (Kay et al., 2015). The atmosphere is modeled with a resolution (grid distance) of 0.9° latitude, 1.25° longitude and 70 vertical layers (up to 140 km or 10^{-6} Pa). Due to the instability of the high emission scenario not all ensemble members of the control run reach the end of the century (Tilmes et al., 2018). The 20 members reach 2030, three reach 2097 and only one ensemble member reaches the end of 2099. All 20 geoengineering ensemble members reach 2100.

Instead of a constant injection of SO_2, the GLENS setup aims at keeping surface temperature conditions at 2020 values. Due to known asymmetries in surface heating with geoengineering (e.g. polar amplification and higher warming in the Northern Hemisphere than the Southern Hemisphere), three surface temperature goals were chosen: global mean temperature (T_0), interhemispheric surface temperature gradient (T_1), and equator-to-pole surface temperature gradient (T_2). The three 2020 values are chosen as the ensemble average from the control run from the period [2015-2025]. At the time not all ensemble members were available, but the result does not significantly differ from the results obtained with fewer members (Tilmes et al., 2018). This optimisation of non-uniform forcing was adapted from Ban-Weiss and Caldeira (2010) by several geoengineering studies (MacMartin et al., 2013; Kravitz et al., 2016). The following reference values were obtained for 2020 (Kravitz et al., 2017):

$$\begin{aligned} T_0^{ref} &= 288.13 \text{ K} \\ T_1^{ref} &= 0.76 \text{ K} \\ T_2^{ref} &= -5.98 \text{ K} \end{aligned} \tag{1}$$

The temperature values are projected into the three 1st Legendre Polynomials, as latitude dependent functions with constant, linear and quadratic behaviour respectively:

$$\begin{aligned} T_0 &= \frac{1}{A}\int_{-\pi/2}^{\pi/2} T(\psi)\ dA \\ T_1 &= \frac{1}{A}\int_{-\pi/2}^{\pi/2} T(\psi)\ \sin\psi\ dA \\ T_2 &= \frac{1}{A}\int_{-\pi/2}^{\pi/2} T(\psi)\ \frac{1}{2}\ (3\ \sin^2\psi - 1)\ dA \end{aligned} \tag{2}$$

Here, ψ is the latitude, $dA = cos\psi\ d\psi$ is the area of the latitude band and $A = 2\pi R_E \int_{-\pi/2}^{\pi/2} dA$ is the total surface area of the earth with R_E as the radius of the earth. The functions $T_0(\psi)$, $T_1(\psi)$ and $T_2(\psi)$ are plotted in Figure 2, from Kravitz et al. (2017). With this experimental setup, the GLENS project proposes to investigate the feasibility and impacts of "controlling" a variable of the climate with geoengineering, rather than studying specific system responses to geoengineering as in GeoMIP experimental setups.

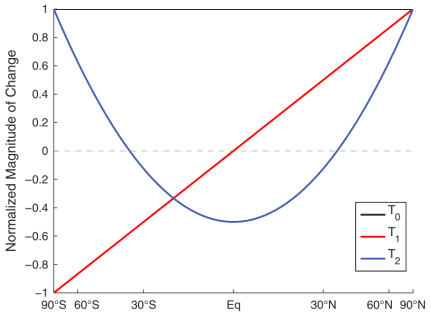

Figure 2. Normalized temperature objectives, as described by Equations (2), as a function of ψ, from Kravitz et al. (2017).

To meet the surface temperature objectives, four degrees of freedom were chosen through *system identification* - the characterization of the input-output relationships in the system (MacMartin et al., 2017). The following four different latitudes of injection were selected: 30°S, 15°S, 15°N, 30°N (coefficients q_{30S}, q_{15S}, q_{15N}, q_{30N}). The injection altitude is fixed at approximately 5 km above the annual mean tropopause. This selection was based in a coarser grid sensitivity experiment, with 10-year simulations for different injection positions (latitude and altitude) as described in Tilmes et al. (2017). The injection longitude was arbitrarily chosen at 180°E, given that atmosphere zonal transport timescale is relatively fast (≈2 weeks). For 1-2°C of cooling, or "low" injection rates, results were found to be approximately linear. Hence, the SO_2 converted aerosol radiative forcing and injection amount are related to aerosol optical depth, by matrix (3):

$$\begin{bmatrix} \mathrm{q}_{30S} \\ \mathrm{q}_{15S} \\ \mathrm{q}_{15N} \\ \mathrm{q}_{30N} \end{bmatrix} = \begin{bmatrix} 20l_1^S + 40l_2 \\ 30(l_0 - (l_1^N + l_1^S + l_2)) + 45l_1^S \\ 30(l_0 - (l_1^N + l_1^S + l_2)) + 45l_1^N \\ 20l_1^N + 40l_2 \end{bmatrix} \tag{3}$$

The factors here presented are obtained from the aforementioned optimisation study from MacMartin et al. (2017). AOD coefficients l_0, l_1 and l_2 are given by (4), and normalised in such a way that, for each ψ, we have $AOD(\psi) = l_0 + l_1 \sin\psi + l_2(3\sin^2\psi)$. Furthermore, $l_1^N = \max(l_1, 0)$ and l_1^S = -min$(l_1, 0)$.

$$\begin{aligned} l_0 &= \frac{1}{A}\int_{-\pi/2}^{\pi/2} AOD(\psi)\ dA \\ l_1 &= \frac{1}{3A}\int_{-\pi/2}^{\pi/2} AOD(\psi)\ \sin\psi\ dA \\ l_2 &= \frac{1}{5A}\int_{-\pi/2}^{\pi/2} AOD(\psi)\ \sin\psi\ \frac{1}{2}\ (3\ \sin^2\psi - 1)\ dA \end{aligned} \tag{4}$$

Constraints to positive injection values and positive gradient values are made. The vector $\vec{l}$ values are related to the surface temperature values (T_0, T_1 and T_2). l and T are related in the following fashion:

$$\begin{bmatrix} T_0 \\ T_1 \\ T_2 \end{bmatrix} \approx \begin{bmatrix} -5.2 & -0.4 & 0.3 & -0.2 \\ -3.7 & -4.4 & 4.3 & -0.2 \\ -2.4 & -2.2 & 1.5 & -1.6 \end{bmatrix} \begin{bmatrix} l_0 \\ l_1^N \\ l_1^S \\ l_2 \end{bmatrix}, \tag{5}$$

where the relation matrix is essentially lower triangular: l_0 affects all temperatures, l_1 affects T_1 and T_2, and l_2 affects mostly T_2. Due to the complexity of the climate system response to the

forcing, this relation is known to be over-simplistic. Linearity of SO_2 injection climate forcing is assumed and the effect of different time-scale responses neglected. Furthermore, an equilibrium state from a 7-year average out of a 10 years run is assumed.

A controller-feedback algorithm is then applied to the model to adjust the injection needed yearly. The feedback is calculated after the feedforward was estimated (the amount needed calculated from the control data results). Therefore, the controller algorithm acts on the residuals, making it more efficient. For each year the feedback is calculated as:

$$l_{i,j+1} = k_p(T_{i,j} - T_{i,ref}) + k_i \sum_{q=1}^{j} (T_{i,q} - T_{i,ref}) \tag{6}$$

k_p and k_i are the proportional and integral factors (the sensitivities of the feedback algorithm), respectively. Index j is the current model year and i=0,1,2 the T and l component index. In spite of the nonlinearities, the algorithm does a good job in keeping with 2020 levels, only slightly deviating for the gradients at the end of the century where it struggles to catch up with the transient run (Tilmes et al., 2018) as shown in Table 2. This implies a slight polar warming as T_2 diverges. Results show a linearity between SO_2 injection and surface temperature response, nevertheless, Kravitz et al. (2018) discusses the possible need to use a more complex aerosol model to capture non-linear aerosol growth behaviour.

Component	Reference	Geoengineering
T_0	288.21 (0.11)	288.24 (0.13)
T_1	0.59 (0.05)	0.62 (0.05)
T_2	6.01 (0.04)	5.94 (0.04)

Table 2. Ensemble standard deviation in brackets. Reference values calculated as the ensemble average between 2015 and 2025 of the Control rum and as the average for the whole period (2020-2100) for the Geoengineering. Results taken from Tilmes et al. (2018).

Thus, to track blocking events in both scenarios, the daily output variables of zonal and meridional wind, and geopotential height at 500 hPa of GLENS are used. From the geoengineering run, the data from three ensemble members for the last decade is used: *Geo* [2090-2100]. In addition, the data from three ensemble members of the control run is used from two periods: $Control(Start)$ [2010-2030] and $Control(End)$ [2090-2099].

2.2. Methods

As presented in the Introduction, blocking events are known to cause a meridional gradient reversal in the mid-latitude gradients, by the intrusion of low-PV (warm) air from the tropics. They can be tracked on the the dynamical tropopause level (2PVU) as the reversal of potential temperature (θ_2) (Pelly and Hoskins, 2003), and as a pressure reversal on the 500 hPa geopotential height (Z500) (Lejenäs and Økland, 1983). Two methods of meridional flow reversal are used: the Tibaldi and Molteni (1990) method (TM90) adapted from Lejenäs and Økland (1983), and a modified TM90 method developed by Barnes et al. (2012). Both methods focus on the reversal of pressure in the Z500 geopotential height. Albeit the θ_2 view is arguably more dynamically significant, Barnes et al. (2012) shows that with her method, both Z500 and θ_2 methods give similar results. The Z500 variable has the advantage of being a standard output variable and frequently available. The following schematic shows the spatial pattern of a reversal, around a central latitude ϕ_c (Figure 3).

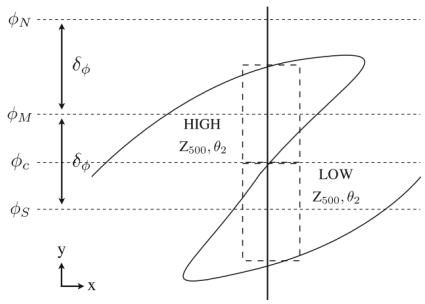

Figure 3. Latitudes associated with flow reversal as defined by Tibaldi and Molteni (1990). Figure from Barnes et al. (2012).

The longitude is then blocked if, at a certain time, the north geopotential height gradient is smaller than a defined quantity W_{min} (negative: low pressure over higher pressure) and the south geopotential gradient bigger than a defined quantity E_{min} (positive: high pressure over low pressure). This is called the instantaneous criteria and if the conditions are met, the longitude is labeled as Instantaneously Blocked Longitude (IBL). The south and north gradients, named Geopotential Height Gradient South (GHGS) and Geopotential Height Gradient North (GHGN) respectively, are calculated as (7).

$$\begin{aligned} GHGS &= \frac{Z(\phi_M) - Z(\phi_S)}{\phi_M - \phi_S} > E_{min} \\ GHGN &= \frac{Z(\phi_N) - Z(\phi_M)}{\phi_N - \phi_M} < W_{min} \end{aligned} \tag{7}$$

The latitudes ϕ_N (north), ϕ_M (mid) and ϕ_S (south) are selected around ϕ_c, and defined as:

$$\begin{aligned} \phi_N &= \left(\phi_c + \frac{3}{2}\delta_\phi\right) + \Delta \\ \phi_M &= \left(\phi_c + \frac{1}{2}\delta_\phi\right) + \Delta \\ \phi_S &= \left(\phi_c - \frac{1}{2}\delta_\phi\right) + \Delta \end{aligned} \tag{8}$$

Here, Δ is a defined latitude shift north and south, in case a block is not exactly located in ϕ_c, and δ_ϕ is the meridional extent of the block. ϕ_c is constant in time in Tibaldi and Molteni and $\phi_c = \phi_c(\lambda)$. In Barnes et al. ϕ_c is defined daily by the climatological average and $\phi_c = \phi_c(t, \lambda)$. This climatological ϕ_c is also called the Daily Central Blocking Latitude (DCBL). Tibaldi and Molteni apply the condition (7) and if a single longitude is blocked for at least five consecutive days, then it is a blocked longitude. Barnes et al. defines a regime behaviour instead of the longitude stationarity criteria, and hence it is called a regime blocking method. To apply the method of Tibaldi and Molteni, the python library *Mid-Latitude Evaluation System (MiLES)* (Davini, 2018), part of the *Earth System Model eValuation Tool (ESMValTool)*, was used. The parameter values used to track the IBL, for each method, are presented in Table 3. It should be noted that MiLES changes the longitude grid size to 2.5° before applying the method here mentioned.

	Tibaldi and Molteni	Barnes et al.
ϕ_c	50°N	DCBL
δ_ϕ	20°	15°
Δ	-5°, 2.5°, 0°, 2.5°, 5°	-5°, 0°, 5°
GHGN	-10 m/°lat	-10 m/°lat
lightgrayGHGS	0 m/°lat	0 m/°lat

Table 3. IBL tracking parameter values used for each method.

In order to find the daily central blocking latitude (DCBL), the Transient Eddy Kinetic Energy (TEKE) at 500hPa is used. It is calculated with the spectrally filtered u_{500} and v_{500}, with a band-pass between 2 and 6 days, as $TEKE = u_{500}^2 + v_{500}^2$. The DCBL is the latitude at which the daily averaged maximum of the TEKE occurs. It is the estimation of the position of the mid-latitude jet, and where the jet blocking might be occurring. Before averaging the daily maxima over the whole period, the TEKE is spatially smoothed with a 3.75° x 2.85° window (x4). Additionally, before taking the latitude of maximum TEKE, the DCBL is filtered in time by taking the mean and the four 1st harmonics and smoothed in space with a 10° window. All ensemble members, both from the control and geoengineering runs, are used to calculate the climatology of the jet (i.e. DCBL).

After the IBLs have been found with the DCBL, Barnes et al. starts by grouping individual IBL, to check if non-consecutive blocked longitudes belong to one or more blocks occurring on the same day. This is done by finding IBL within 7.5° of another IBL, labelling the longitudes in between as IBL and if the group of longitudes has a width of at least 15°, then it is labelled as a group of instantaneously blocked longitudes (GIBL). If this minimum width is not met, the grouped longitudes are discarded as a potential block. To belong to the same blocking event, the GIBL needs to overlap at least 10° with a consecutive day GIBL, and the center of the blocked longitudes can not be advected more than 45° in a day. If an event persists for 5 days, it is labelled a regime block. A Hovmöller diagram of a tracked regime block is displayed in Figure 4 and the corresponding Z500 fields for the tracked days in Figure 5.

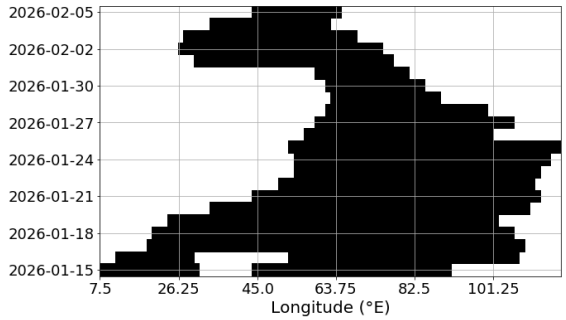

Figure 4. Hovmöller diagram of a tracked blocking event, or regime blocking, tracked with the described methodology by Barnes et al. (2012).

However, not all meridional gradient reversals are associated with the blocking of the jet stream, and Figure 6 shows a schematic of the possible cases, as presented in section 1. The importance of knowing the jet position as not to track wave breaking in the poleward region of the jet, reveals the importance of finding an accurate DCBL.

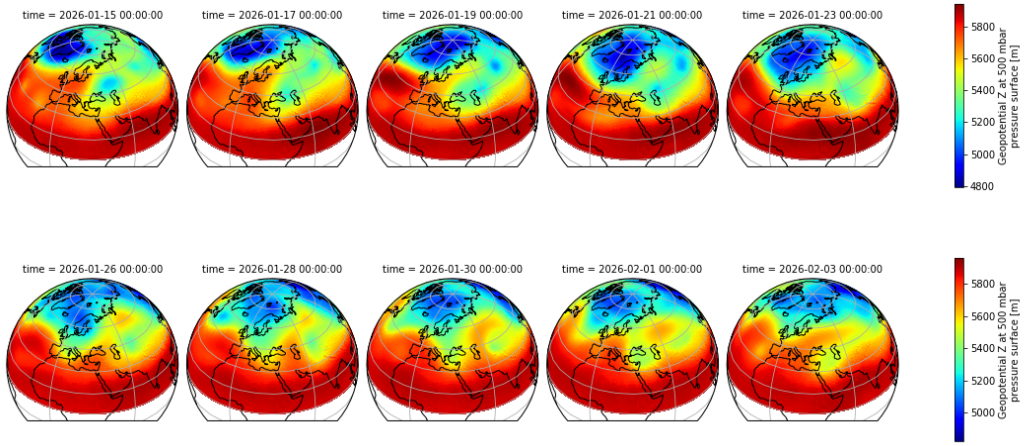

Figure 5. Z500 fields of a tracked blocking event, or regime blocking, tracked with the described methodology by Barnes et al. (2012).

Nevertheless, a definition of a DCBL for a long time series, with several associated time scale effects, is not without issues. If the jet stream moves poleward, as predicted by models with increasing GHG emission, the climatological DCBL is pushed northward and the tracking can occur on the poleward side of the jet, therefore identiying cases of wave breaking as blocks. Other methods have been proposed, and MiLES library has the 2-D extension of the Tibaldi and Molteni by Davini et al. (2012) available. The 2-D methods have the advantage of not relying on a climatological DCBL but are more prone to picking up wave breaking events on the poleward region of the jet. For this reason, in addition to the Barnes et al. method, the method of Tibaldi and Molteni, with a fixed central latitude, is also applied to the time series.

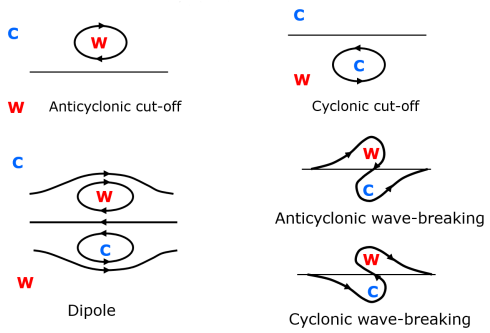

Figure 6. Meridional gradient reversal events, from Hoskins (2007).

To assess the differences in mean state, the North Annular Mode (NAM) index is used. As described in section 1, the NAM index is defined as the normalised difference of zonal mean sea level pressure (SLP) between 35°N and 65°N. For the comparison of intensity of change in the different scenarios and seasons, the NAM index used is not normalised and simply calculated with the anomalies for the full period:

$$NAM_i = \left([P]_{35,i} - \overline{[P]}_{35}\right) - \left([P]_{65,i} - \overline{[P]}_{65}\right), \tag{9}$$

where $[P]$ is the zonal mean sea level pressure for period i (year) and $\overline{P}$ the mean over the number of periods.

Due to the small number of ensemble members used for this project, significance is calculated with a non-parametric method (A/B testing). The test compares the difference between sample groups A and B. The original difference (R_0) is compared with the difference of the reshuffled

(R_n), or randomly split, A/B from the full sampling pool (A+B). If group A has N_A samples (A_i=$A_1, ..., A_{NA}$) and group B has N_B samples (B_i=$B_1, ..., B_{NB}$), the difference is calculated as:

$$R = \frac{1}{N_A}\sum_{i=0}^{N_A} A_i - \frac{1}{N_B}\sum_{i=0}^{N_B} B_i \tag{10}$$

N_S reshuffles are made and the differences R_n ($R_1, ..., R_N$) calculated. R_0 is significant at S% if the original R_0 is greater/smaller than $100\% - \frac{S}{2}\%$ (two-tailed), and confidence is (100-S)% (Wieners et al., 2016). The number of shuffles N_S is selected so that significance converges, i.e. if $S(N_S) = S(\frac{N_S}{2})$. All Geo and Control ensembles (full variability range) are used for confidence calculations.

3. Results and Discussion

In this section, the results of blocking tracking are presented, for both Tibaldi and Molteni (1990) and Barnes et al. (2012) methods. In section 3.1, the general differences in behaviour between the Control(RCP8.5) and Geoengineering ensembles are presented. The seasonal variation is shown in section 3.2, while the typical size and duration of blocks is covered in section 3.3.

Before proceeding to the blocking tracking results, is important to look at the general dynamics of the simulation. The approximate behaviour of the eddy driven jet (EDJ) can be partly inferred through the analysis of the calculated Daily Central Blocking Latitude (DCBL). Figure 7 shows the DCBL climatology for all ensemble members (Control+Geo) in panel (a), and for each of the three separate periods studied here: Control [2010-2030] in (b), Control [2090-2097] in (c) and Geo [2090-2100] (d). The DCBL shows the typical seasonality of the jet, moving poleward in the summer and southward in the winter, and the typical meandering in longitude in winter months, with troughs downstream of the Rocky Mountains and the Himalayas. DCBL in (a) is used to track blockings on all periods, and it varies between 33.7°N to 75°N. The result is very similar to Barnes et al. (2012) for ERA40 reanalysis data, also with a maximum region of DCBL in the summer around 100°E, at the Pacific storm track entrance.

Since the period from (b) has more years than (c) and (d), it is not surprising that it is the most similar to (a), with a spatial σ^2=1.2°. The End Control period (c), having a maximum at 78°N and minimum at 40°N, differs up to 15° from (a) in the Pacific region, making it the most deviated (σ^2=3.8°). From the lack of ensemble members and years, it is hard to tell if this is a result of internal variability or a slight poleward trend as predicted by some GCMs under increased CO_2 scenarios. Nevertheless, Richter et al. (2018) shows that Eddy Kinetic Energy (EKE) strengthens in the middle latitudes at 700hPa, with a general intensification and eastward expansion in the Atlantic storm track region, and slightly shifting poleward in the Pacific, for RCP8.5 simulations (See Figure 7 of Richter et al. (2018)). The same trend is not seen in the Geo members, with weakening westerlies and mostly negative EKE anomalies in the mid-latitudes, with the exception of increased zonal wind in the British isles-North Sea and Northern Europe region. This is also in agreement with the DCBL results here presented. Moreover, albeit the used DCBL (a) being slightly equatorward/poleward in the Pacific, it is still not more than Δ displaced from (c) or (d).

Furthermore, GCMs are known to have strong storm track and EDJ associated bias, badly predicting eddy jet position and strength in comparison with reanalysis (Mitchell et al., 2017). This has been shown to strongly correlate with Rossby wave breaking and blocking position (Woollings et al., 2010). The Atlantic jet exhibits a trimodal behaviour, typically picking between 3 latitudes (37°N, 45°N and 58°N), with the southern mode being typically associated with Scandinavia

and Greenland (60°W-15°W) blocking at higher latitudes, and the northern mode connected to British isles and North Sea blocks. Mitchell et al. (2017) shows that GCMs from CMIP5, including CESM1(CAM5), badly match with reanalysis data in this aspect. Particularly, Kwon et al. (2018) shows that in the large ensemble project of CESM1(CAM5) (CESM1LE), the EDJ exhibits a quadmodal behaviour, with the 3 preferred modes too close from each other and too northerly from the observed data, and concentrating more towards the central ones for the end of the RCP8.5 simulation, with a stronger and eastward elongated storm track (through Europe). This eastward expansion is also seen in the GLENS RCP8.5 scenario, on par with the strengthening and poleward shift of the jet under climate warming scenarios of CMIP5 GCMs (Barnes and Polvani, 2013). It should be noted that the geoengineering run also follows a RCP8.5 emission scenario and not all GHG effects are offset by Geoengineering, and in the Northern Atlantic Simpson et al. (2019) finds a northward jet shift in winter.

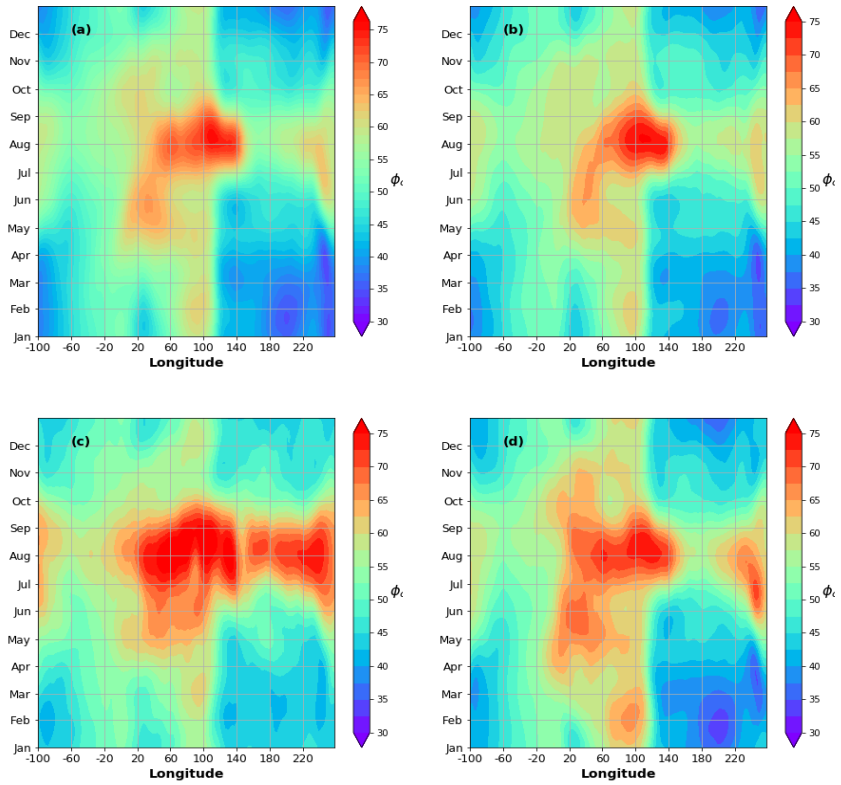

Figure 7. Annual variation of the Daily Central Blocking Latitude (ϕ_c) calculated for: all periods (a), Control [2010-2030] (b), Control [2090-2097] (c), and Geo [2090-2100] (d). Latitude ϕ_c in degrees north and Longitude in degrees east.

In the tropics, under the geoengineering scenario, there is heating between the region of injections and the tropopause (30-100hPa), in the cold point tropopause, due to aerosol absorption. The middle and upper stratosphere cool due to decreased SW heating from ozone depletion and aerosols albedo. With the increased meridional stratospheric temperature gradient, the extratropical stratospheric jets intensify (up to 8 ms^{-1}). The extratropical westerlies in the lower stratosphere and upper troposphere (in the upper region of the subtropical jet) are weakened, and anomalous easterlies are seen in the tropical stratosphere, a pattern associated with the easterly phase of the QBO (see Figures 4 and 5 in Richter et al. (2018)). The polar vortex changes less than 2 ms^{-1} for control, while it strengthens up to 4 ms^{-1} in the Geo simulations and exhibits amplified extreme states (from -20 to 60 ms^{-1}). Moreover, Richter et al. (2018) finds that the polar jet also strengthens

for the geoengineering ensemble and the number of Sudden Stratospheric Warming events (SSWs) does not significantly differ between Control and Geo (but both significantly decrease in relation to the historic run).

3.1. Blocking Frequency

The number of blocking events per year is shown in Figure 8. Panels (a) and (b) show the results using the Barnes et al. method (BSW), with the climatological DCBL, while (c) and (d) are obtained with a fixed EDJ latitude of 50°N, with the Tibaldi and Molteni (1990) method (TM). Overall, the TM method tracks more blocks than BSW. This arises not only due to not having any longitudinal regime constraints, but also because the method is not dependent on EDJ behaviour. The method weaknesses are then associated with the fixed latitude tracking, with detection of systems associated with (anomalous) southerly displaced persistent cut-off lows and of subtropical and subpolar anticyclones (Barriopedro et al., 2010). Panels (a) and (c) compare the yearly number of blocks in the Control for the last years [2090-2097] and the first [2010-2030]. The Control (Start) has more yearly events than Control (End), confidence 95% for (a) and 99% confidence for (c). In (b) and (d) we can compare the Geo yearly trend with the same period in the Control [2090-2097]. Geo has more yearly events than Control (End), confidence 99% for (b) and (c). The same can be said about Geo having more yearly blocks than Control (Start), with 99% confidence for both methods. These results show that blocking occurrence is overall increased in the geoengineering scenario ensemble members against both control periods.

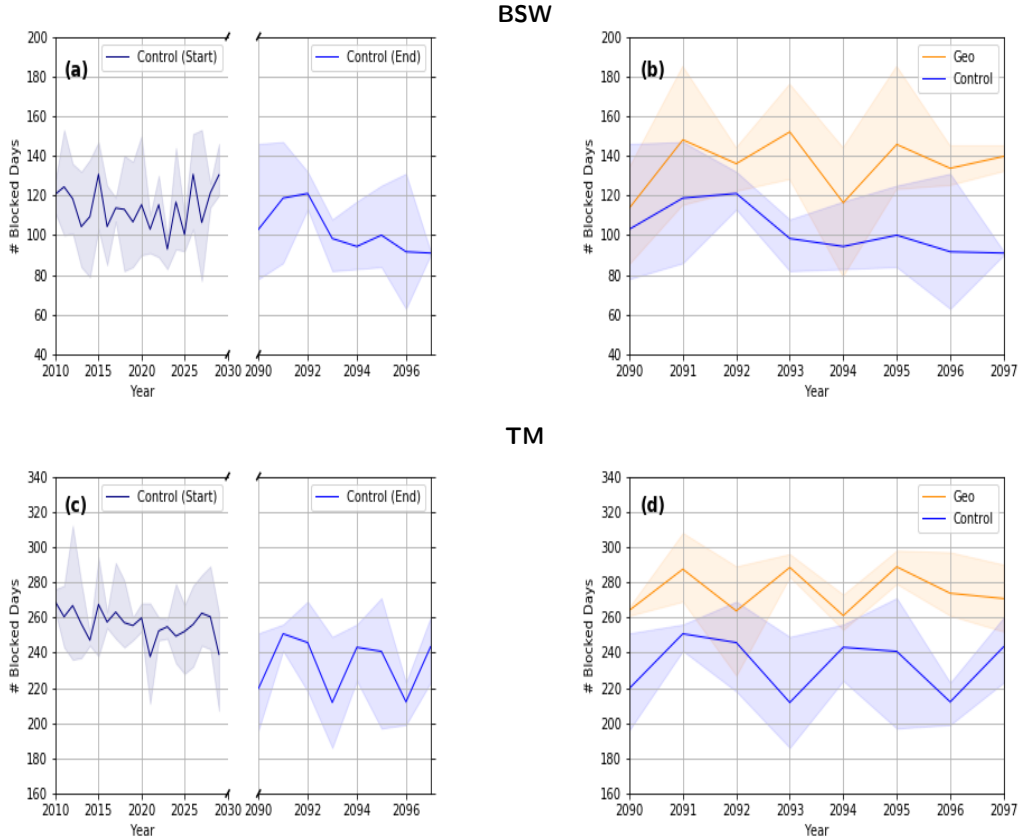

Figure 8. Number of blocked days per year, for both Barnes et al. (a, b) and Tibaldi and Molteni(c, d) methods. Thick lines represent ensemble average, and shading ensemble variation. Panels to the left (a, c) represent both Control run periods [2010-2030] and [2090-2097], and panels to the right (b, d) the last years [2090-2097] of Control and Geo runs.

Models underestimate blocking occurrence, and its behaviour depends on the model mean state bias and resolution. Blocking has three preferential locations: European (15W-25E), Greenland (15W-60W) and Pacific (150°W-150°E). Figures 9 and 10 show the frequency of blocks per longitude, for Geo versus Control [2090-2097], and Control [2010-2030] versus Control [2090-2097], respectively. Panels (a) and (c) show the longitudinal distribution of the blocking frequency for each method, while the right panels (b) and (d) show the correspondent ensemble mean differences per longitude. BSW method has a more noticeable peak between 0 and 50°E (European Sector) and a smaller one around between 210°E–240°E (Eastern Pacific), corresponding to the two jet exit regions. With the TM method, the Pacific peak, between 150°E and 200°E (Central Pacific), is stronger than the European one, between -50° and 30°E (Atlantic - Western Europe). Hence, the peaks with the TM method are more westward centered in comparison with BSW. This is due to the previously mentioned weakness of the method in tracking the anticyclones of the subtropical high pressure belt (Azores and Pacific). The two peak locations with the TM (around 0° and 180°) and BSW (25° and 225°) methods are also the same captured by the method with reanalysis data. One feature that seems to be missing from the BSW method results is the Greenland blocking, typically associated with poleward cyclonic Rossby wave breaking, when the jet is in a southern mode. Moreover, as the jet shifts poleward, anticyclonic wave breaking shifts with the jet while the cyclonic does not (Barnes and Polvani, 2013). Due to a decrease in background vorticity gradient and the critical line being nearer on the equatorward side, wave breaking then occurs mostly on the equatorward side. Kwon et al. (2018) finds indeed that, in RCP8.5 CESM, most blocking events occur in fact south of the jet, when the EDJ is in a northward mode. A strong jet is associated with inhibited wave breaking events, due to jet core wave entrapment and refraction (Barnes and Hartmann, 2011). In GLENS, further investigation into this wave breaking, jet preferred mode and blocking interaction is still required. Moreover, High-latitude blocks do not obstruct the jet but rather displace it equatorward (Barnes and Hartmann, 2011). Despite the inherit weaknesses of the methods, and the shortcomings of modeled blocking in comparison to observations, comparing differences within the same method still can give useful insight into dynamical changes.

There is no significant difference in peak location or in distribution between the three periods. As detected for annual number of blocks, Geo is overall bigger than Control (End) and Control (Start) across all longitudes, as can be seen in (b) and (d), with 99% confidence for both methods and periods. The same happens, albeit less strongly, for the control run, with less events toward the end of the century than the start (97% confidence for BSW and 99% for TM). The slightly lower confidence in the hypothesis stated is due to Control (End) being bigger than Control (Start) between approximately 50°E and 100°E. The peak mentioned, is due to autumn and winter blocking behaviour in this region, that then averages to the shown distributions in Figure 9 and 10. Locally, in regions of low frequency, differences may be slightly negative due to the lack of representation (low blocking occurrence) and not significant.

In conclusion, there is an overall increase, across all longitudes, of blocking in the geoengineering scenario. This is likely connected to the EKE differences between the RCP8.5 control simulation and Geo. At the end of the RCP8.5, the jet is stronger and mostly zonal, with positive anomalies in the westerlies, associated with inhibition of wave breaking, while Geo exhibits a weakening in relation to the start period. This strengthened/weakened jet effect can be compared in the computed yearly or DJF "NAM" (as described in the methods), in Figures 11, or the traditional (stronger correlated) winter mode, in Figure 12. Mean sea level pressure in (a) diverges through the control run. The Geo SLP value at 35°N becomes slightly lower, at 65° remains around the same. These changes in mean sea level pressure lead to a slightly negative NAM trend for Geo and a positive trend for control (b). Under a positive NAM the EDJ becomes more zonal, meanders less, and

strengthens (increased pressure gradient and thermal wind balance). Hence, NAM negative modes have been associated with increased meridional mass flux (wave breaking), increase in mixing and decrease in meridional gradients, and with an increase in blocking events. It is always hard to disentangle cause and effect in mean state and eddy activity interaction, but nevertheless they exhibit a strong correlation.

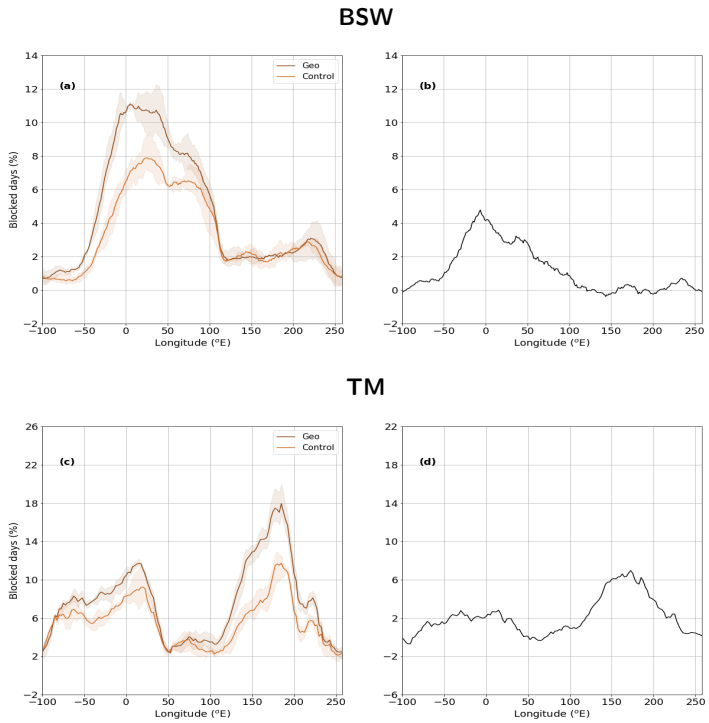

Figure 9. Blocking frequency, per longitude, using the method by Barnes et al. (2012) (a) and Tibaldi and Molteni (1990) (c). Thick lines represent the ensemble average and shading the ensemble variability. The difference Geo minus Control (End) of ensemble average, for each method (from the left), in the right panels (c, d). Averages for the period [2090-2097].

The surface temperature gradient difference is not enough to explain these blocking changes, as shown by the idealised GCM experiment by Hassanzadeh et al. (2014), and eddy dynamics play a relevant role. Furthermore, Simpson et al. (2019) compares the GLENS results to an idealised experiment of stratospheric heating in the same model (GEOHEAT), and shows that stratospheric heating is the dominant factor in the changes in zonal wind and storm track (weakening) in the Geo experiment. This connection has been demonstrated in several idealized experiments. Nevertheless, the storm track is weakened, and shifted, with greater extent than with only stratosphere heating, hinting at the importance of GHG, aerosols and other diabatic distribution changes. Further investigation into the mechanisms that drive these changes is still required, in particular into the stratosphere-troposphere connection. Dallasanta et al. (2019) finds the importance of (surface) eddies for this connection, instead of the typical stronger polar vortex view, through another idealised experiment.

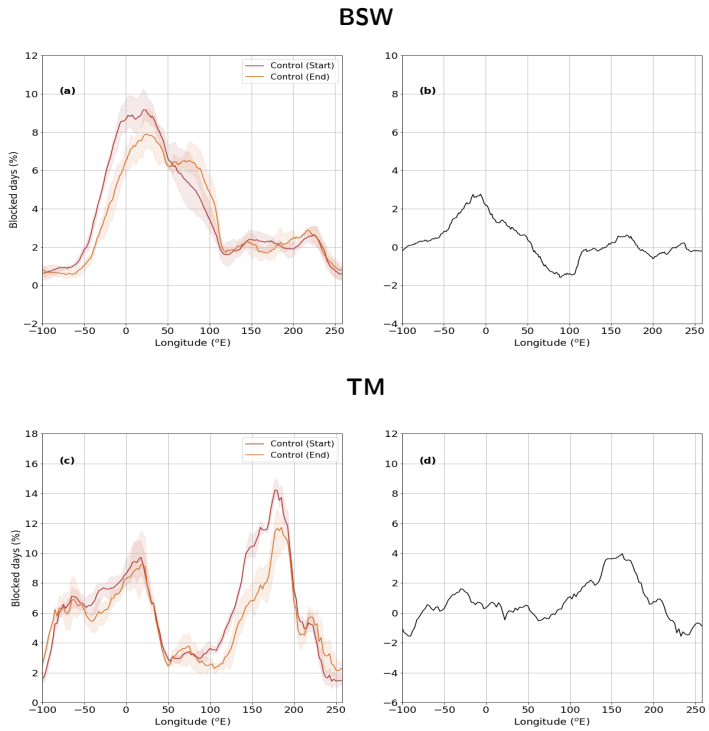

Figure 10. Blocking frequency, per longitude, using the method by Barnes et al. (2012) (a) and Tibaldi and Molteni (1990) (c). Thick lines represent the ensemble average and shading the ensemble variability. The difference Control (Start) minus Control (End) of ensemble average, for each method (from the left), in the right panels (b, d). Averages for Control (End) from the period [2090-2097], and Control (Start) from [2010-2030].

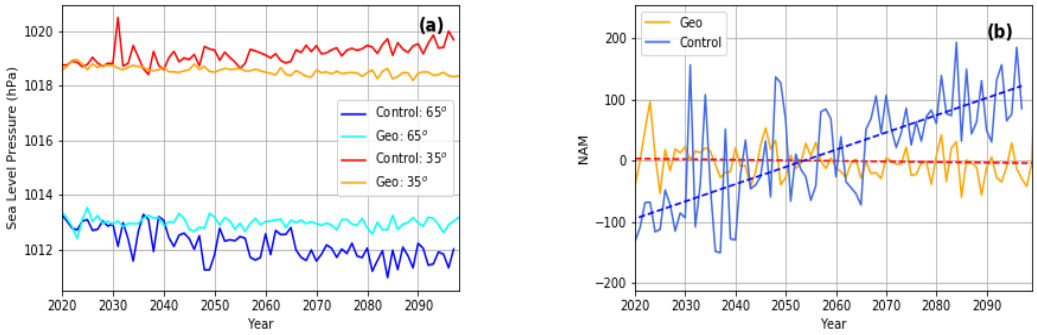

Figure 11. Zonal mean of annual mean sea level pressure at 35° and 65° (a), and respective North Annular Mode (b), for the period [2020-2100]. Dashed lines represent the NAM linear trend. Control run values end in 2098.

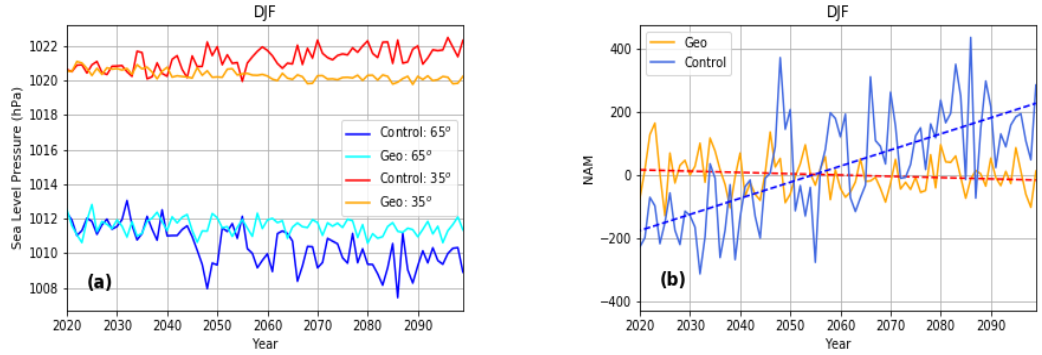

Figure 12. Zonal mean of winter (DJF) mean sea level pressure at 35° and 65° (a), and respective North Annular Mode (b), for the period [2020-2100]. Dashed lines represent the NAM linear trend. Control run values end in 2098.

3.2. Blocking Seasonal Variation

Similar to the previous section, as to compare the three periods, the Geo, Control (End) and Control (Start) are shown for all seasons, for both methods. The henceforth mentioned differences are not aimed at inferring on geographical impacts of geoengineering, but rather to take notice of the behavioural changes under the different scenarios, in the model.

As seen for the average distribution by longitude in the previous section, blocking frequency increases significantly with geoengeneering in relation to control (End) in both BSW and TM, for all seasons except summer (Figures 13, 14, 15 and 16), with 99% confidence. In both Geo and the start of the control run [2010-2030], spring (MAM) is the season with the most blocking events, for both methods (Figures 14 and 18). Spring is the season with most events for TM method in the later control years [2090-2097] too, while for BSW summer blocking becomes the most frequent (Figure 19a), mostly due to a decrease in frequency for all other seasons (while summer remained around the same frequency).

For autumn (SON), in Figure 16a, there seems to be a shift of the Atlantic peak towards the Atlantic, similar to what happens early in the control run (Figure 20a). This could be related to an increase in Greenland blocking tracking as the climatological jet moves northward. Winter (Figure 13) and Spring (Figure 13) are the seasons where there is a stronger increase in blocking in the European sector under geoengineering.

For DJF, MAM and SON the Geo frequency is higher than control (start), albeit with some regional variation, with both methods (95% confidence). Summer has a very distinct behaviour for both methods. In the control, in Figure 19a (BSW), there are more blocking events occurring between the two peaks of Europe and Pacific, which appears to be reduced around 50°E (Scandinavia) with geoengineering (Figure 19). Figure 15b (TM), shows the inverse behaviour, stronger in the control in the Atlantic region and a stronger Geo peak in the Pacific, with the same happening when compared to the control start (Figure 19b).

With the TM method, in all periods, the number of blocks in MAM is greater, followed by DJF, JJA and SON. With the BSW method, MAM and SON have more blocks in the start of control and with Geo, but fewer for control end. It is also interesting to notice that the Pacific peak is always stronger in TM (as is the European in BSW) except for winter (Figures 13b and 17b). The differences in winter (TM) might be related to less stationary systems in the basins, in comparison to other seasons. In Figures 17a and 13a (BSW), there is a westward shift in the Pacific peak.

The seasonal changes between start and end of the control are more subtle than with geoengineering (Figures 17, 18, 19 and 20). Spring and autumn (Figures 18 and 20) still display the blocking reduction for the control scenario (99% confidence). These changes are in the range of ensemble variability, but still significant. In Figure 20a, there are still local increases around 50°E to 100°E and 220°E and a slight shift to the East (as previously mentioned).

Furthermore, there seems to be similar behaviour between Geo and Control (Start), associated with a weaker jet, while the control (End) blocks are more eastward shifted and likely associated with a stronger jet, further downstream.

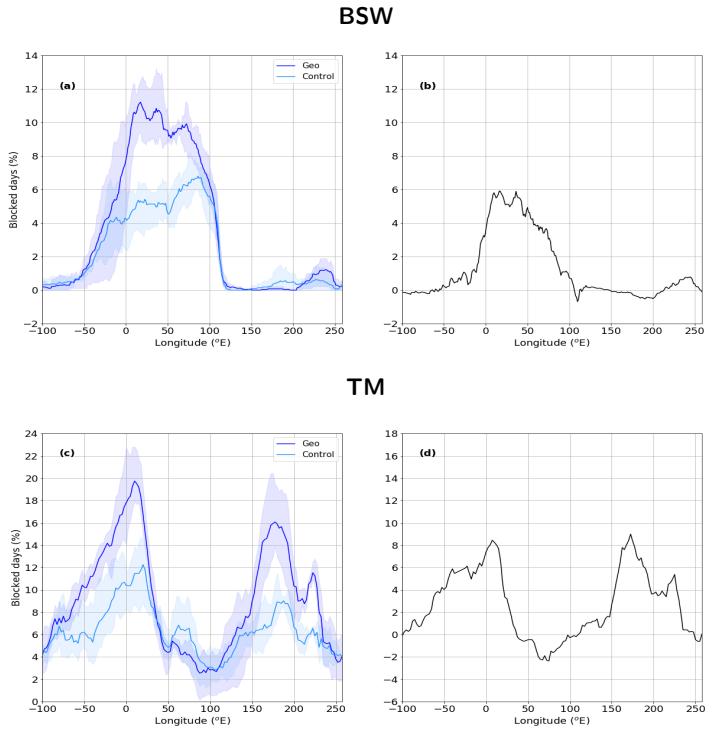

Figure 13. Blocking Seasonal average for winter (DJF), per longitude, using the method by Barnes et al. (2012) (a) and Tibaldi and Molteni (1990) (c). Thick lines represent the ensemble average and shading the ensemble variability. The difference Geo minus Control (End) of ensemble average, for each method (from the left), in the right panels (b, d). Averages for the period [2090-2097]

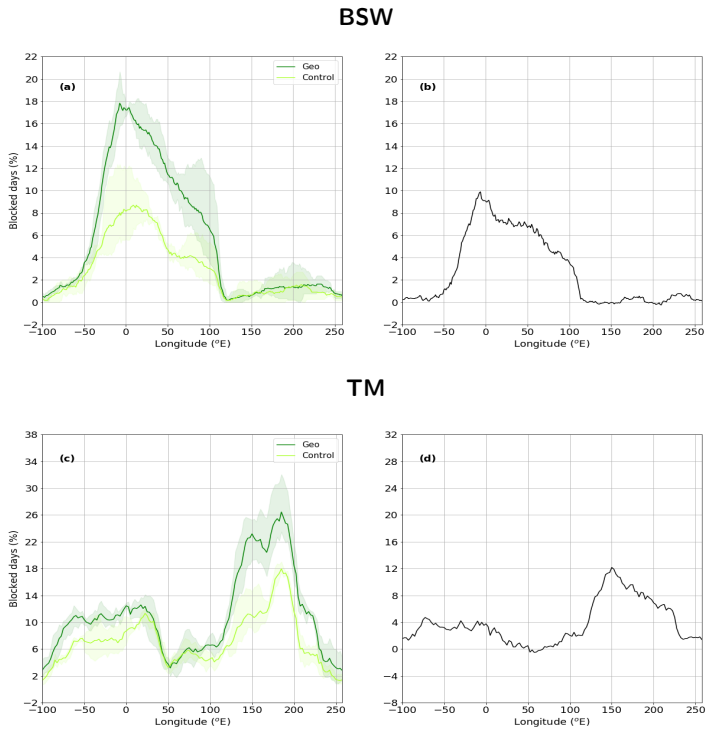

Figure 14. Blocking seasonal average for spring (MAM), per longitude, using the method by Barnes et al. (2012) (a) and Tibaldi and Molteni (1990) (c). Thick lines represent the ensemble average and shading the ensemble variability. The difference Geo minus Control (End) of ensemble average, for each method (from the left), in the right panels (b, d). Averages for the period [2090-2097]

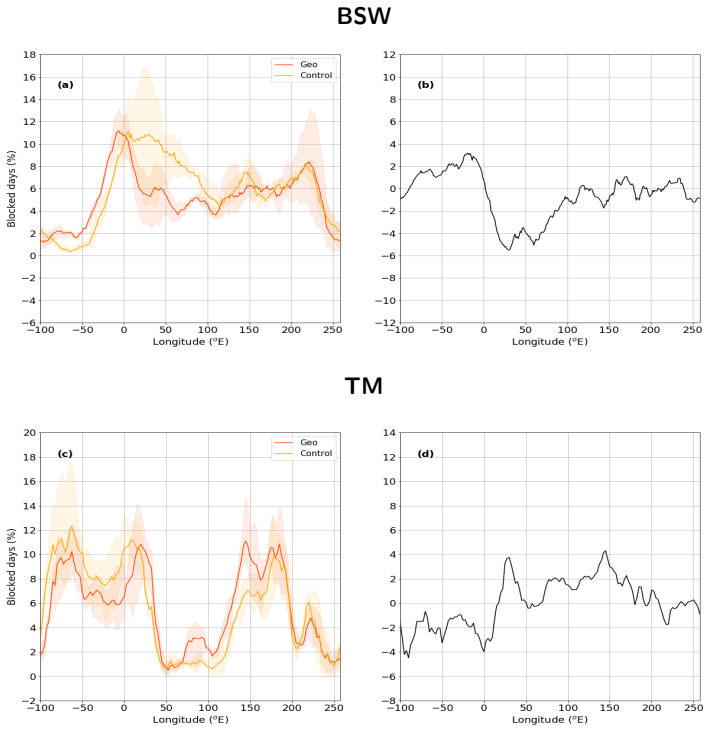

Figure 15. Blocking seasonal average for summer (JJA), per longitude, using the method by Barnes et al. (2012) (a) and Tibaldi and Molteni (1990) (c). Thick lines represent the ensemble average and shading the ensemble variability. The difference Geo minus Control (End) of ensemble average, for each method (from the left), in the right panels (b, d). Averages for the period [2090-2097]

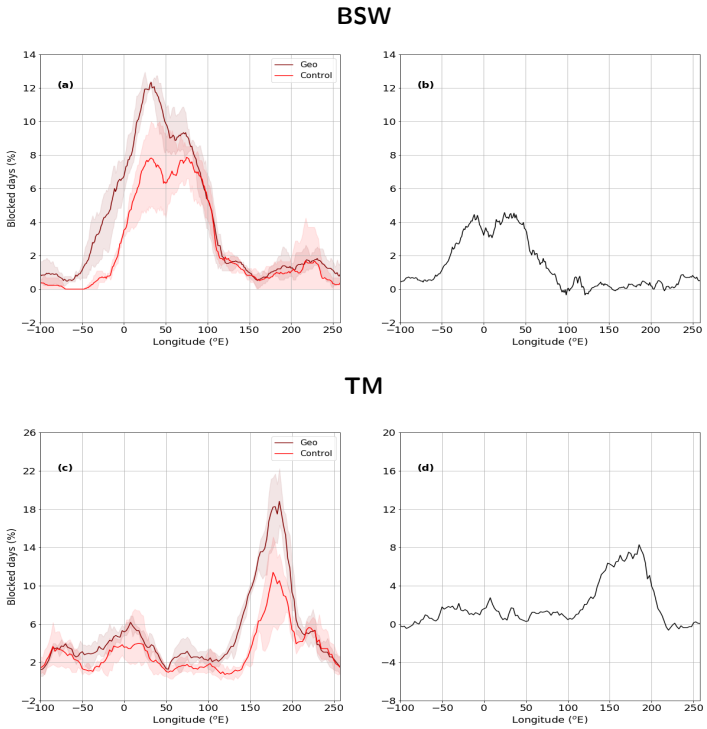

Figure 16. Blocking seasonal average for autumn (SON), per longitude, using the method by Barnes et al. (2012) (a) and Tibaldi and Molteni (1990) (c). Thick lines represent the ensemble average and shading the ensemble variability. The difference Geo minus Control (End) of ensemble average, for each method (from the left), in the right panels (b, d). Averages for the period [2090-2097]

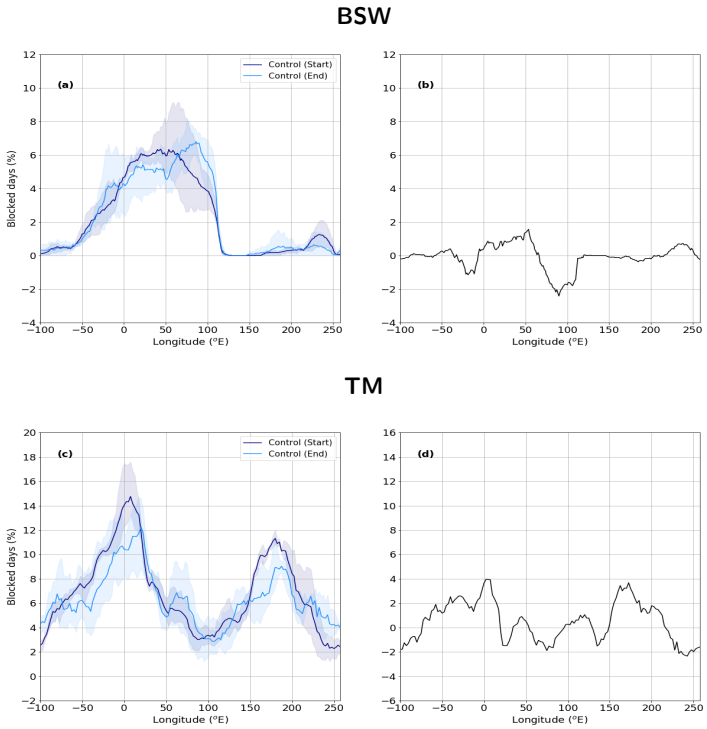

Figure 17. Blocking seasonal average for winter (DJF), per longitude, using the method by Barnes et al. (2012) (a) and Tibaldi and Molteni (1990) (c). Thick lines represent the ensemble average and shading the ensemble variability. The difference Control (Start) minus Control (End) of ensemble average, for each method (from the left), in the right panels (b, d). Averages for Control (End) from the period [2090-2097], and Control (Start) from [2010-2030].

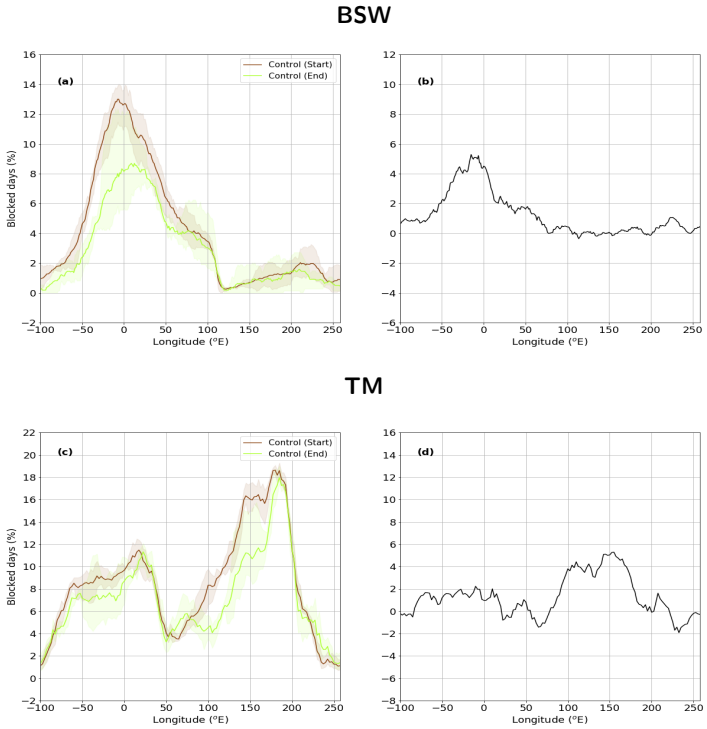

Figure 18. Blocking seasonal average for spring (MAM), per longitude, using the method by Barnes et al. (2012) (a) and Tibaldi and Molteni (1990) (c). Thick lines represent the ensemble average and shading the ensemble variability. The difference Control (Start) minus Control (End) of ensemble average, for each method (from the left), in the right panels (b, d). Averages for Control (End) from the period [2090-2097], and Control (Start) from [2010-2030].

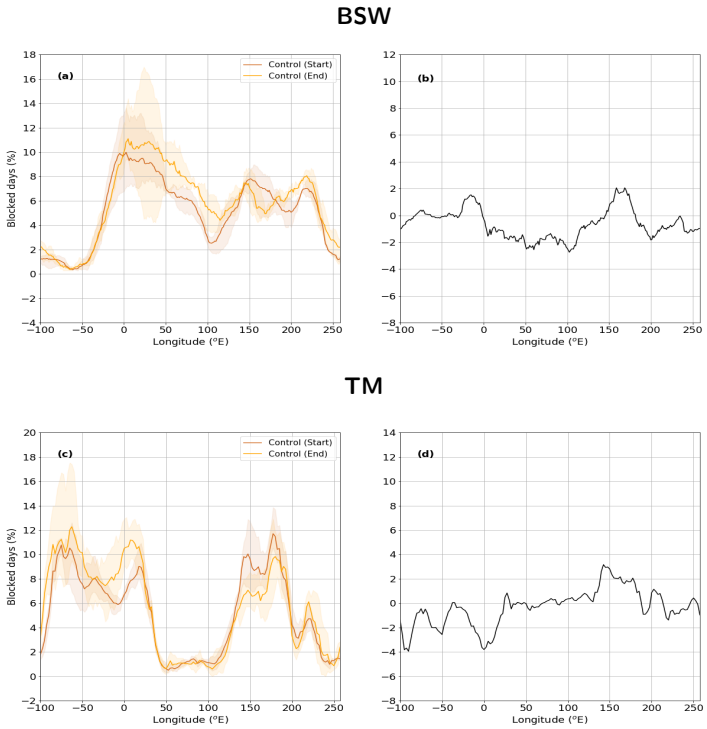

Figure 19. Blocking seasonal average for summer (JJA), per longitude, using the method by Barnes et al. (2012) (a) and Tibaldi and Molteni (1990) (c). Thick lines represent the ensemble average and shading the ensemble variability. The difference Control (Start) minus Control (End) of ensemble average, for each method (from the left), in the right panels (b, d). Averages for Control (End) from the period [2090-2097], and Control (Start) from [2010-2030].

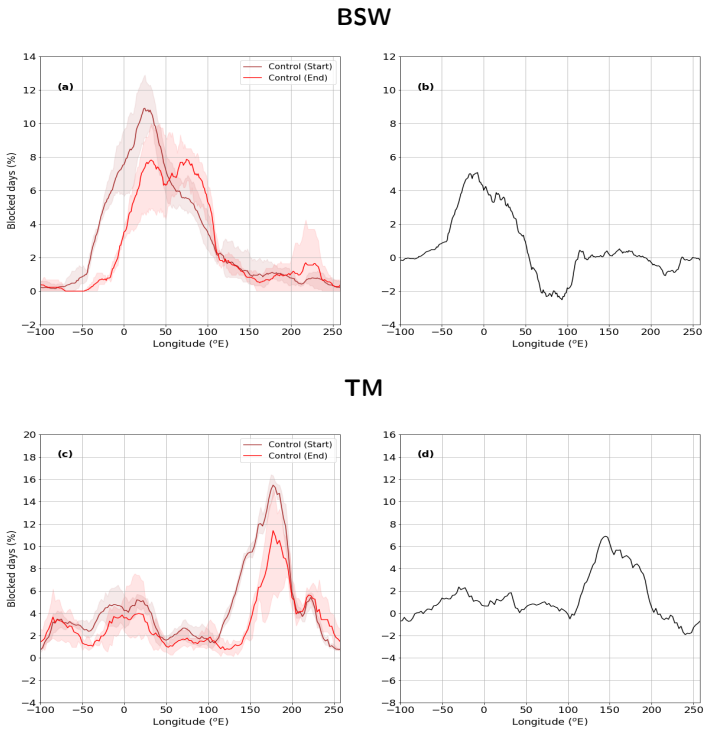

Figure 20. Blocking seasonal average for autumn (SON), per longitude, using the method by Barnes et al. (2012) (a) and Tibaldi and Molteni (1990) (c). Thick lines represent the ensemble average and shading the ensemble variability. The difference Control (Start) minus Control (End) of ensemble average, for each method (from the left), in the right panels (b, d). Averages for Control (End) from the period [2090-2097], and Control (Start) from [2010-2030].

3.3. Blocking Extension and Duration

The method by Barnes et al. (2012) tracks blocking events, which allows the study of the typical longitude extension and duration. Figure 21 shows the distribution of duration for the three studied periods. The duration exhibits an exponential behaviour, decaying with a rate λ, with most events persisting for 5-10 days. This bias towards the reproduction of short-lived events is present in GCMs in the CMIP5, which includes CESM(CAM5), as shown by Mitchell et al. (2017). The same bias seems to also be present in CESM(WACCM). Furthermore, there is no significant trend in the unfitted data: Control (Start) is not significantly higher than Control (End), with only 50% confidence; and Geo is not significantly higher than the same period Control (End) distribution, with only 45% confidence.

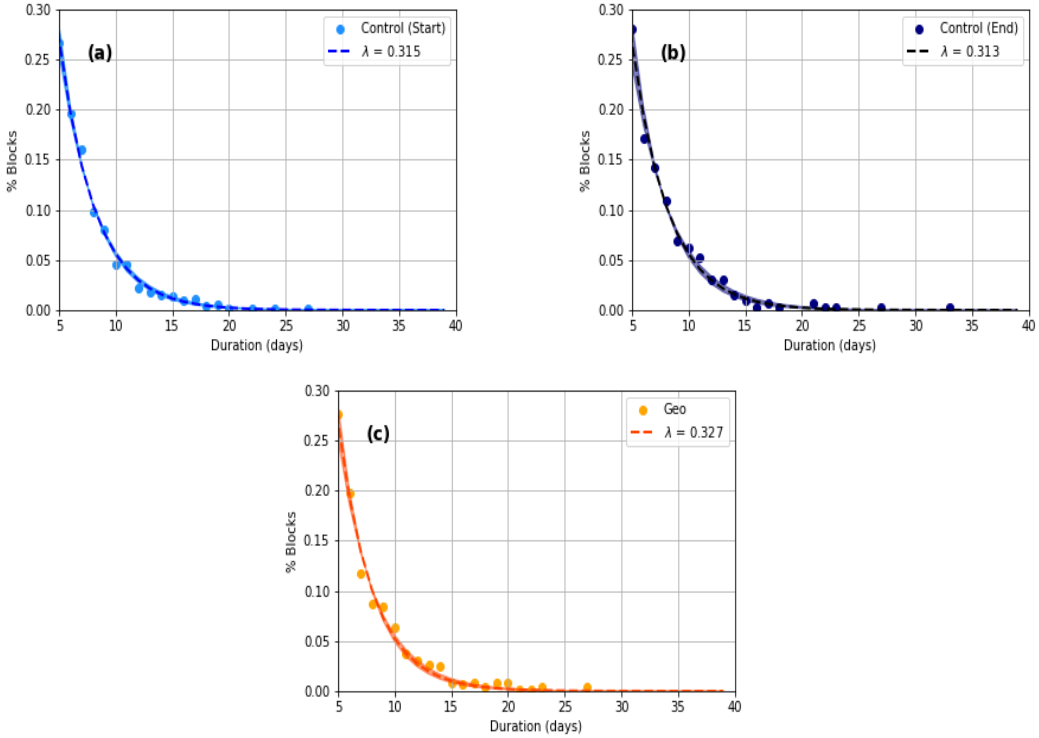

Figure 21. Blocking duration statistics in days, for all ensemble members. Control (Start) [2010-2030] (a), Control (End) [2090-2097] (b), and Geo [2090-2100] (c). Points represent the data distribution. Dashed lines represent the exponential distribution fit shaded for 95% confidence interval of lambda (rate) estimation.

The extension statistics are investigated by looking at the daily blocked longitudes during blocking events. Figure 22 shows the probability density functions (PDF) for the daily extension. Most blocked days have between 25° to 75° longitudes blocked. Figure 22(d) shows the three estimated PDFs, estimated using a non-parametric method, with a Gaussian kernel density estimator. There is no trend in the (unfitted) extension behaviour between the start and end periods of Control (36% confidence that Start > End), or between geoengineering and control (25% confidence that Geo > Control). Typically, longer events (time) tend to affect more longitudes (space) (Barnes et al., 2012) and Figure 21 shows that duration decays very fast in the tracked events, making the larger events more unlikely. The geoengineering distribution (with more events tracked than the others) is better represented, but the extremes are still badly represented (short periods), making it hard to infer on the change in extreme occurrences, i.e. the likelihood of a large/persistent block occurring under the geoengineering scenario versus the control.

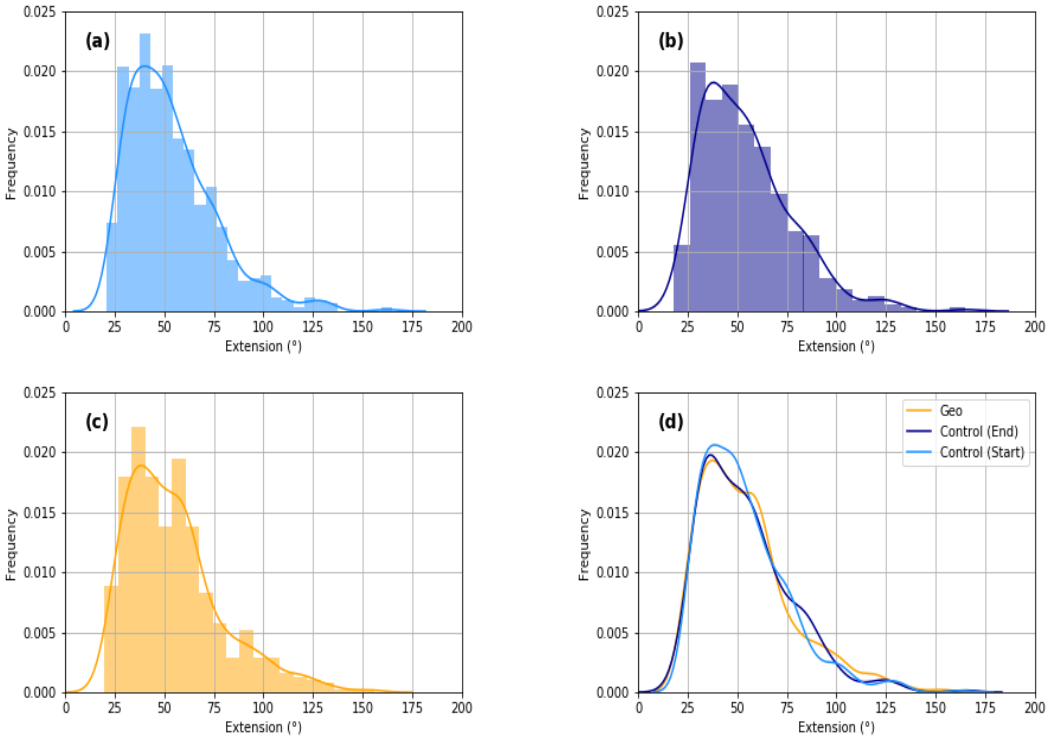

Figure 22. Daily blocking longitude extent (°) statistics, for all ensemble members, for Control (Start) [2010-2030] (a), Control (End) [2090-2097] (b), and Geo [2090-2100] (c), all periods (d). Probability density function estimated with non-parametric Gaussian Kernel Distribution Estimator (KDE). Kernel bandwidth estimated with Silverman's method and equal to 5° (a), 6° (b) and 5.5° (c). Bin width calculated using Freedman-Diaconis rule and equal to 5°(a), 6°(b), and 8° (c).

4. Conclusion

This GLENS experimental setup gives useful insights into changed blocking behaviour, but understanding its weaknesses and uncertainties is important. Accurate blocking reproduction in models is still not achieved, connected with the lack of a comprehensive theory behind blocking events (Woollings et al., 2018). Nevertheless, the reasonable reproduction of blocking at jet exits gives some hope into the improvement of model reproduction. GCMs have a strong mean state bias and the changes here found are likely linked to the changed the mean state (Scaife et al., 2010). Simpson et al. (2019) finds that the stratospheric warming is the key factor in dynamical changes, but the mechanism by which the troposphere and stratosphere are connected is still uncertain. Planetary waves and transient eddies as mechanisms have been proposed for this. Furthermore, the North Atlantic storm track is influenced by the AMOC (Woollings et al., 2012), that considerably strengthens in GLENS (Fasullo et al., 2018). In spite of that the increased ocean heat transport northward is accompanied by a decrease in atmosphere heat transport. The low values of Greenland blocking and the indistinguishable number of SSW event frequency that occur in both scenarios could point to a lack of accuracy in jet locations and stratospheric wave breaking. The eddy jet positions still require higher resolution models (Schiemann et al., 2017) and improved orography (Berckmans et al., 2013). Nevertheless, Kwon et al. (2018) and (Mitchell et al., 2017) show than not always a resolution increase improves the quality of blocking modelling. Furthermore, physical mechanisms behind eddy jet shift poleward under climate change is still weakly understood (Menzel et al., 2019).

George Box used to write "all models are wrong, but sometimes they can be useful", which rings true for climate studies, and in particular to such a potentially harmful endeavour as geoengineering. CESM(WACCM) is currently the best method for stratospheric aerosol geoengineering studies but predicting extreme events with current state GCMs is still inadvisable. In spite of this, in this project, we find a strong connection between EDJ strength and blocking occurrence in the Northern Hemisphere, mainly in the European Sector, tracked by the BSW method. As to eliminate the dependence on the climatological DCBL definition (but not more accurate), the TM method is also used. The TM method results show the same overall increase in blocking frequency. Blocking increases significantly with geoengineering in the last model years in comparison to the same period control scenario run, and it even increases globally in relation to the start of the control run. This response is analogous to the weakening of EKE and westerlies in the middle to high latitudes in geoengineering. While westerlies become weaker in geoengineering, strengthening of westerlies and EKE occurs through the control scenario (Simpson et al., 2019). This interaction is captured by the zonal mean sea level pressure variation, with a "more negative NAM" for geoengineering versus a "more positive NAM" in the control run. Seasonal behaviour mostly shows the same response with the exception of summer, for the control versus geoengineering for the last years. Moreover, there is no significant change in the persistence and extent with geoengineering.

The question of the impacts with this increased blocking frequency remains open. There is a global precipitation suppression, but with lower surface temperatures versus the control scenario, return times of "extreme temperatures" might be lower. Furthermore, with a high vertical resolution, and changed stratospheric dynamics, it would be potentially interesting to investigate the relationship between wave breaking and blocking frequency and location in GLENS.

References

Ban-Weiss, G. A. and Caldeira, K. (2010). Geoengineering as an optimization problem. *Environmental Research Letters*, 5(3).

Barnes, E. A. and Hartmann, D. L. (2011). Rossby wave scales, propagation, and the variability of eddy-driven jets. *Journal of the Atmospheric Sciences*, 68(12):2893–2908.

Barnes, E. A. and Polvani, L. (2013). Response of the midlatitude jets, and of their variability, to increased greenhouse gases in the CMIP5 models. *Journal of Climate*, 26(18):7117–7135.

Barnes, E. A., Polvani, L. M., and Sobel, A. H. (2013). Model projections of atmospheric steering of Sandy-like superstorms. *Proceedings of the National Academy of Sciences of the United States of America*, 110(38):15211–15215.

Barnes, E. A., Slingo, J., and Woollings, T. (2012). A methodology for the comparison of blocking climatologies across indices, models and climate scenarios. *Climate Dynamics*, 38(11-12):2467–2481.

Barriopedro, D., García-Herrera, R., and Trigo, R. M. (2010). Application of blocking diagnosis methods to General Circulation Models. Part I: A novel detection scheme. *Climate Dynamics*, 35(7):1373–1391.

Berckmans, J., Woollings, T., Demory, M.-E., Vidale, P.-L., and Roberts, M. (2013). Atmospheric blocking in a high resolution climate model: influences of mean state, orography and eddy forcing. *Atmospheric Science Letters*, 14(1):34–40.

Dallasanta, K., Gerber, E. P., and Toohey, M. (2019). The circulation response to volcanic eruptions: The key roles of stratospheric warming and eddy interactions. *Journal of Climate*, 32(4):1101–1120.

Davini, P. (2018). Miles - mid latitude evaluation system.

Davini, P., Cagnazzo, C., Gualdi, S., and Navarra, A. (2012). Bidimensional diagnostics, variability, and trends of northern hemisphere blocking. *Journal of Climate*, 25(19):6496–6509.

Fasullo, J. T., Tilmes, S., Richter, J. H., Kravitz, B., MacMartin, D. G., Mills, M. J., and Simpson, I. R. (2018). Persistent polar ocean warming in a strategically geoengineered climate. *Nature Geoscience*, 11(12):910–914.

Hassanzadeh, P., Kuang, Z., and Farrell, B. F. (2014). Responses of midlatitude blocks and wave amplitude to changes in the meridional temperature gradient in an idealized dry gcm. *Geophysical Research Letters*, 41(14):5223–5232.

Hoskins, B. (2007). Blocking and Rossby Wave-breaking [PowerPoint slides]. Retrieved from `http://www.cgd.ucar.edu/events/webcasts/blackmon-symposium/`.

Kay, J. E., Deser, C., Phillips, A., Mai, A., Hannay, C., Strand, G., Arblaster, J. M., Bates, S. C., Danabasoglu, G., Edwards, J., Holland, M., Kushner, P., Lamarque, J. F., Lawrence, D., Lindsay, K., Middleton, A., Munoz, E., Neale, R., Oleson, K., Polvani, L., and Vertenstein, M. (2015). The community earth system model (CESM) large ensemble project : A community resource for studying climate change in the presence of internal climate variability. *Bulletin of the American Meteorological Society*, 96(8):1333–1349.

Kravitz, B., MacMartin, D. G., Mills, M. J., Richter, J. H., Tilmes, S., Lamarque, J. F., Tribbia, J. J., and Vitt, F. (2017). First simulations of designing stratospheric sulfate aerosol geoengineering to meet multiple simultaneous climate objectives. *Journal of Geophysical Research: Atmospheres*, 122(23):12,616–12,634.

Kravitz, B., MacMartin, D. G., Wang, H., and Rasch, P. J. (2016). Geoengineering as a design problem. *Earth System Dynamics*, 7(2):469–497.

Kravitz, B., Robock, A., Boucher, O., Lawrence, M., Moore, J. C., Niemeier, U., Storelvmo, T., Tilmes, S., and Wood, R. (2018). The Geoengineering Model Intercomparison Project–introduction to the second special issue.

Kwon, Y.-O., Camacho, A., Martinez, C., and Seo, H. (2018). North atlantic winter eddy-driven jet and atmospheric blocking variability in the community earth system model version 1 large ensemble simulations. *Climate Dynamics*, 51(9):3275–3289.

Lejenäs, H. and Økland, H. (1983). Characteristics of northern hemisphere blocking as determined from a long time series of observational data. *Tellus A*, 35 A(5):350–362.

Lenton, T. M. and Vaughan, N. E. (2009). The radiative forcing potential of different climate geoengineering options. *Atmospheric Chemistry and Physics*, 9(15):5539–5561.

Li, J. and Wang, J. X. (2003). A modified zonal index and its physical sense. *Geophysical Research Letters*, 30(12):1–4.

Luo, D. (2005). Why is the North Atlantic block more frequent and long-lived during the negative NAO phase? *Geophysical Research Letters*, 32(20):1–5.

MacMartin, D. G., Keith, D. W., Kravitz, B., and Caldeira, K. (2013). Management of trade-offs in geoengineering through optimal choice of non-uniform radiative forcing. *Nature Climate Change*, 3(4):365–368.

MacMartin, D. G. and Kravitz, B. (2019a). Mission-driven research for stratospheric aerosol geoengineering. *Proceedings of the National Academy of Sciences of the United States of America*, 116(4):1089–1094.

MacMartin, D. G. and Kravitz, B. (2019b). The Engineering of Climate Engineering. *The Annual Review of Control, Robotics, and Annu. Rev. Control Robot. Auton. Syst*, 2:445–467.

MacMartin, D. G., Kravitz, B., Tilmes, S., Richter, J. H., Mills, M. J., Lamarque, J. F., Tribbia, J. J., and Vitt, F. (2017). The climate response to stratospheric aerosol geoengineering can be tailored using multiple injection locations. *Journal of Geophysical Research: Atmospheres*, 122(23):12,574–12,590.

Matsueda, M. (2011). Predictability of Euro-Russian blocking in summer of 2010. *Geophysical Research Letters*, 38(6):1–6.

Menzel, M. E., Waugh, D., and Grise, K. (2019). Disconnect Between Hadley Cell and Subtropical Jet Variability and Response to Increased CO2. *Geophysical Research Letters*, 46(12):7045–7053.

Mills, M. J., Richter, J. H., Tilmes, S., Kravitz, B., MacMartin, D. G., Glanville, A. A., Tribbia, J. J., Lamarque, J. F., Vitt, F., Schmidt, A., Gettelman, A., Hannay, C., Bacmeister, J. T., and Kinnison, D. E. (2017). Radiative and chemical response to interactive stratospheric sulfate aerosols in fully coupled CESM1(WACCM). *Journal of Geophysical Research: Atmospheres*, 122(23):13,061–13,078.

Mills, M. J., Schmidt, A., Easter, R., Solomon, S., Kinnison, D. E., Ghan, S. J., Neely, R. R., Marsh, D. R., Conley, A., Bardeen, C. G., and Gettelman, A. (2016). Global volcanic aerosol properties derived from emissions, 1990–2014, using CESM1(WACCM). *Journal of Geophysical Research*, 121(5):2332–2348.

Minnis, P., Harrison, E., Stowe, L., Gibson, G., denn, F., Doelling, D., and Smith, W. (1993). Radiative climate forcing by the mount pinatubo eruption. *Science (New York, N.Y.)*, 259:1411–5.

Mitchell, D., Davini, P., Harvey, B., Massey, N., Haustein, K., Woollings, T., Jones, R., Otto, F., Guillod, B., Sparrow, S., Wallom, D., and Allen, M. (2017). Assessing mid-latitude dynamics in extreme event attribution systems. *Climate Dynamics*, 48(11):3889–3901.

Pelly, J. L. and Hoskins, B. J. (2003). A new perspective on blocking. *Journal of the Atmospheric Sciences*, 60(5):743–755.

Rex, D. F. (1950). Blocking Action in the Middle Troposphere and its Effect upon Regional Climate: I. An Aerological Study of Blocking Action. *Tellus*, 2(3):196–211.

Richter, J. H., Tilmes, S., Glanville, A., Kravitz, B., MacMartin, D. G., Mills, M. J., Simpson, I. R., Vitt, F., Tribbia, J. J., and Lamarque, J. F. (2018). Stratospheric Response in the First Geoengineering Simulation Meeting Multiple Surface Climate Objectives. *Journal of Geophysical Research: Atmospheres*, 123(11):5762–5782.

Scaife, A. A., Woollings, T., Knight, J., Martin, G., and Hinton, T. (2010). Atmospheric blocking and mean biases in climate models. *Journal of Climate*, 23(23):6143–6152.

Schiemann, R., Demory, M.-E., Shaffrey, L. C., Strachan, J., Vidale, P. L., Mizielinski, M. S., Roberts, M. J., Matsueda, M., Wehner, M. F., and Jung, T. (2017). The resolution sensitivity of northern hemisphere blocking in four 25-km atmospheric global circulation models. *Journal of Climate*, 30(1):337–358.

Simpson, I., Tilmes, S., Richter, J., Kravitz, B., MacMartin, D., Mills, M., Fasullo, J., and Pendergrass, A. (2019). The regional hydroclimate response to stratospheric sulfate geoengineering and the role of stratospheric heating. *Journal of Geophysical Research: Atmospheres*, page 2019JD031093.

Tibaldi, S. and Molteni, F. (1990). On the operational predictability of blocking. *Tellus A*, 42(3):343–365.

Tilmes, S., Richter, J. H., Kravitz, B., MacMartin, D. G., Mills, M. J., Simpson, I. R., Glanville, A. S., Fasullo, J. T., Phillips, A. S., Lamarque, J. F., Tribbia, J., Edwards, J., Mickelson, S., and Ghosh, S. (2018). CESM1(WACCM) stratospheric aerosol geoengineering large ensemble project. *Bulletin of the American Meteorological Society*, 99(11):2361–2371.

Tilmes, S., Richter, J. H., Mills, M. J., Tribbia, J. J., MacMartin, D. G., and Vitt, F. (2017). Sensitivity of Aerosol Distribution and Climate Response to Stratospheric SO 2 Injection Locations Special Section :.

van Delden, A. (2017). Atmospheric dynamics [reader]. retrieved from `http://www.staff.science.uu.nl/~delde102/AtmosphericDynamics.htm`.

Vial, J., Osborn, T. J., and Lott, F. (2013). Sudden stratospheric warmings and tropospheric blockings in a multi-century simulation of the IPSL-CM5A coupled climate model. *Climate Dynamics*, 40(9-10):2401–2414.

Wieners, C. E., de Ruijter, W. P., Ridderinkhof, W., von der Heydt, A. S., and Dijkstra, H. A. (2016). Coherent tropical Indo-Pacific interannual climate variability. *Journal of Climate*, 29(11):4269–4291.

Woollings, T., Barriopedro, D., Methven, J., Son, S. W., Martius, O., Harvey, B., Sillmann, J., Lupo, A. R., and Seneviratne, S. (2018). Blocking and its Response to Climate Change. *Current Climate Change Reports*, 4(3):287–300.

Woollings, T., Gregory, J. M., Pinto, J. G., Reyers, M., and Brayshaw, D. J. (2012). Response of the North Atlantic storm track to climate change shaped by ocean-atmosphere coupling. *Nature Geoscience*, 5(5):313–317.

Woollings, T., Hannachi, A., and Hoskins, B. (2010). Variability of the North Atlantic eddy-driven jet stream. *Quarterly Journal of the Royal Meteorological Society*, 136(649):856–868.